Computational Condensed Matter 16 (2019) e00379

Contents lists available at ScienceDirect

Computational Condensed Matter

journal homepage: http://ees.elsevier.com/cocom/default.asp

Predictions of bandgap and subbands of $\gamma-Al_2O_3$ in presence of intrinsic point defects by DFT+TB-mBJ

M. Yazdanmehr [a], S. Jalali-Asadabadi [a, *], J. Nematollahi [a], A. Nourmohammadi [b], Iftikhar Ahmad [c, d]

[a] Department of Physics, Faculty of Sciences, University of Isfahan (UI), Hezar Gerib Avenue, Isfahan, 81746-73441, Iran
[b] Department of Nanotechnology Engineering, Faculty of Advanced Sciences and Technologies, University of Isfahan, 81746-73441, Iran
[c] Center for Computational Materials Science, University of Malakand, Chakdara, Pakistan
[d] Vice Chancellor Abbottabad University of Science and Technology, Abbottabad, Pakistan

ARTICLE INFO

Article history:
Received 31 July 2018
Received in revised form
1 March 2019
Accepted 2 March 2019

Keywords:
Point defect
Subbands
DFT
Vacancy

ABSTRACT

The electronic structure of γ-Al_2O_3 in the presence of the *Al* and *O* defects is investigated within the density functional theory using the PBE-GGA and TB-mBJ schemes. The formation of the *Al* vacancy produces acceptor-like sublevels above the valence band maximum, consistent with the previous G_0W_0 calculations. Furthermore, the formation of the oxygen vacancy generates donor-like sublevels below the conduction band minimum, which is consistent with experiment. The donor sublevels are predicted more accurately by TB-mBJ than PBE-GGA, as electron charge density is calculated to be larger at the *O* vacancy site by TB-mBJ within its optimized c-factor.

1. Introduction

Recently, alumina as one of the most important ceramic materials with exceptional properties has attracted considerable attention [1–8]. The effects of the intrinsic point defects on the electronic structures are of significant importance [9–12], because they can substantially influence the electronic structures of γ-Al_2O_3 [13–15]. However, the theoretical studies to date are mainly devoted to the hypothetical ideal γ-Al_2O_3 which cannot be unambiguously generalized to the real case containing intrinsic point defects, and theoretical studies on the electronic structure of the real case are rare [16–21]. Although the physical properties of the hypothetical structure has been already explored by the *ab initio* calculations, the electronic structure of the real case have not been systematically studied. γ-Al_2O_3 is an attractive solid material in nanotechnology due to its extensive use as a catalyst, an adsorbent, a support for industrial catalysts, and a pH-sensitive membrane [22–26]. It is also considered as a blocking dielectric for advanced nonvolatile memories [27–29] such as TANOS ($TaN(TiN)/Al_2O_3/Si_3N_4/SiO_2/Si$) charge storage devices [30,31], which are designed for the next generation high density terabit flash memories [32,33]. The electronic structure, bandgap, conduction band offset, dielectric constant, and optical properties of this material have been studied theoretically [34–43] by considering an ideal hypothetical structure for the compound. It is difficult to synthesize the ideal γ-Al_2O_3 in a laboratory and in practice an experimentally synthesized γ-Al_2O_3 usually contains different point defects including oxygen and/or aluminum vacancies [31,44–46]. The electronic structures of these defects play an important role in the stability and technological applications of γ-Al_2O_3 [36,47,48]. The point defects can create additional sharp bands, called subbands, somewhere between the valence band maximum (VBM) and conduction band minimum (CBM) [21,31,49,50]. Hence, the positions of these subbands in γ-Al_2O_3 have been studied experimentally [31,50] and theoretically [49] by G_0W_0 method. TB-mBJ method [51] is a semilocal method and thereby nearly as fast as the standard LDA and consequently suitable for heavy supercell calculations. Our last study [41], using TB-mBJ method [51] revealed that the bandgap of the ideal γ-Al_2O_3 compound could be effectively predicted by the non-regular TB-mBJ method. Here following our recent study on the optical properties of this compound [21], we would extend our last study [41] by considering a real crystal structure of γ-Al_2O_3, while starting from the ideal crystal structure as a reference to realize the effects

* Corresponding author.
E-mail address: sjalali@sci.ui.ac.ir (S. Jalali-Asadabadi).

https://doi.org/10.1016/j.cocom.2019.e00379
2352-2143/

of the defects. Then, the defects are simulated by removing (forming) some *Al* and *O* atoms (vacancies) with different coordination numbers in the ideal γ-Al_2O_3 structure using DFT + TB-mBJ. It is observed that the relative positions of the extra subbands are in complete accordance with the experimental results [50]. The formation of *Al* vacancy generates acceptor-like subbands which are also in agreement with the previous G_0W_0 results [49]. Our results in agreement with experiment [50] show that the formation of oxygen vacancy generates donor-like subbands below the CBM. The higher accuracy of the TB-mBJ method originates from the fact that electron charge density at the *O* vacancy site is predicted to be higher by the non-regular TB-mBJ than by the regular TB-mBJ and PBE-GGA. The physics behind of the latter result is discussed by analyzing the electron charge density.

2. Crystal structure of $\gamma-Al_2O_3$

2.1. Ideal defective spinel structure

The disagreement over the crystal structure of γ-Al_2O_3 has not been solved yet because of low crystallinity of this compound and different procedures as well as the precursor materials which have been used for the synthesis [36,52]. In this study, we consider the defective spinel model and utilize the optimized structure obtained previously [36,41] for the ideal γ-Al_2O_3. The ideal γ-Al_2O_3 crystallizes in the defective spinel structure $\square_{2\frac{2}{3}}Al_{21\frac{1}{3}}O_{32}$, where "□" symbol stands for the *Al* vacancy to satisfy the stoichiometry of the formula [34]. The empty box symbol is called the stoichiometric *Al* vacancy. This defective spinel structure can be obtained from the perfect spinel structure $Mg_8Al_{16}O_{32}$ by replacing *Mg* with *Al*, which results in $Al_{24}O_{32}$ (see Fig. 1(a)). We divide the $Al_{24}O_{32}$ by 4, which yields Al_6O_8 (see Fig. 1(b)). Then, we multiply Al_6O_8 by 3. This gives $Al_{18}O_{24}$ which is identical to put three Al_6O_8 unit cells on top of each other, as shown in Fig. 1(c). We now subtract 2 Al atoms from $Al_{18}O_{24}$ to reach a triclinic structure of $\square_2Al_{16}O_{24}$ (see Fig. 1(d)). We have subtracted those aluminum atoms which have been located in the octahedral sites due to the lowest energy configuration of the constructed γ-Al_2O_3 system as compared to those of the other 13 possible configurations (for details see Refs. [34,41]). The $\square_2Al_{16}O_{24}$ structure can be considered as a triclinic unit cell for the defective spinel structure. This structure is called alumina. For practical simplicity, we transform the oblique triclinic unit cell to a hexagonal unit cell, see Ref. [36]. The hexagonal structure, as shown in Fig. 1 (e), is the primitive unit cell that we have used for the ideal γ-Al_2O_3 compound (see Ref. [35]).

2.2. Intrinsic point defects in the defective spinel structure

In principle, the ideal structure of γ-Al_2O_3 can be constructed, as discussed in Sec. 2.1. The physical properties of the ideal structure are calculated [41], but in reality the ideal crystal cannot be synthesized in a laboratory. In practice, γ-Al_2O_3 contains *Al* or *O* intrinsic point defects [31,44,47]. These point defects can change the electronic structure of the system. Thus, it may be crucial to create the crystal structure in the presence of these point defects. In order to simulate the intrinsic point defects, we introduce *Al* or *O* vacancy by removing *Al* or *O* atom from the ideal structure. There are two different types of aluminum (oxygen) atoms in the ideal structure. The type of *Al* (*O*) depends on its point group symmetry, which can be distinguished by its coordination numbers. The coordination numbers can be 4 (3) or 6 (4) for *Al* (*O*), see the ideal structure as shown in Fig. 1 (e) to count the coordination numbers. After removing *Al* (*O*) atom from the ideal structure, an *Al* (*O*) vacancy is formed in the position of the removed *Al* (*O*) atom. The *Al* (*O*) vacancy is denoted as V_{Aln} (V_{On}), where *n* can be 4 (3) or 6 (4) to indicate the coordination numbers of the removed *Al* (*O*) atom. The V_{Al4} and V_{Al6} vacancies are shown in Fig. 2(a) and (b), respectively. It is important to note that the V_{Al4} and V_{Al6} vacancies are different from the stoichiometric *Al* vacancy, as discussed in Sec. 2.1 and denoted by an empty box "□". Similarly, the two types of *O* vacancies V_{O3} and V_{O4} are shown in Fig. 2(c) and (d), respectively. V_{Al4}, V_{Al6}, V_{O3} and V_{O4} are our used intrinsic point defects, while their structures are given in Fig. 2(a) and (b), (c) and (d), respectively.

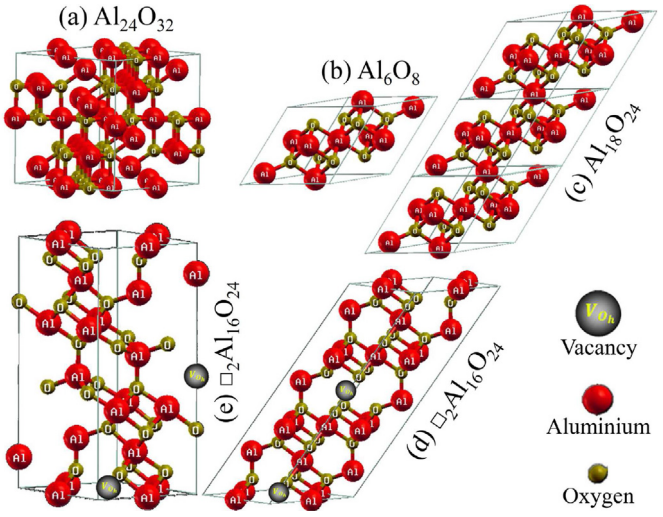

Fig. 1. "(color online)" (a) Perfect spinel structure $Al_{24}O_{32}$, (b) Primitive unit cell Al_6O_8 of the perfect spinel structure, (c) Ideal triclinic spinel structure γ-$Al_{18}O_{24}$, (d) Ideal defective triclinic spinel structure γ- $\square_2Al_{16}O_{24}$, (e) Ideal defective hexagonal spinel structure γ- $\square_2Al_{16}O_{24}$. The "□" symbol stands for the stoichiometric *Al* vacancy.

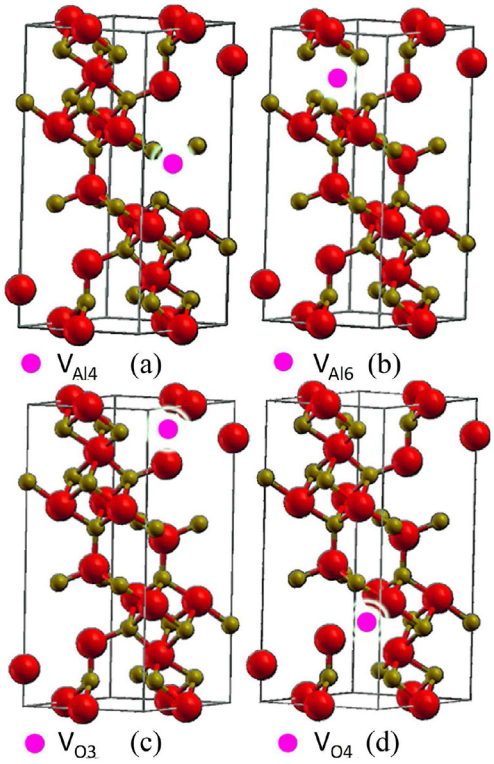

Fig. 2. "(color online)" Defective hexagonal spinel structure in the presence of the intrinsic point defects (a) V_{Al4}, (b) V_{Al6}, (c) V_{O3}, and (d) V_{O4}. V stands for vacancy and numbers are used to show the coordination numbers.

The total number of atoms in the supercell constructed for this study is 40. The number of intrinsic *O* or *Al* vacancies regardless of the coordination numbers in the supercell is one, *viz.* the number of V_{Al} or V_O is 1. As aforementioned in the last Sec. 2.1, the supercell also contains two stoichiometric *Al* vacancies at octahedral (O_h) site, *viz.* the number of $V_{Al@Oh}$ is 2. Hence, our supercell either contains one intrinsic (non-stoichiometric) *O* vacancy and two stoichiometric *Al* vacancies or contains one intrinsic (non-stoichiometric) *Al* vacancy and two stoichiometric *Al* vacancies. The concentration of lattice defects is defined to be $c = n/N$, where n is the number of defects and N is the total number of atoms [53]. Thus, the intrinsic *O* defect concentration, $c(V_O) = 1/40 = 0.025 = 2.5\%$, is equal to the intrinsic *Al* concentration, $c(V_{Al}) = 2.5\%$, while it is equal to half of the stoichiometric *Al* concentration at the O_h site, $c(V_{Al@O_h}) = 2/40 = 0.05 = 5\%$. Therefore, the ratio of the non-stoichiometric *O* and the stoichiometric *Al* defect concentrations, $c(V_O)/c(V_{Al@O_h}) = 0.5$, is equal to the ratio of the non-stoichiometric *Al* and stoichiometric *Al*, $c(V_{Al})/c(V_{Al@O_h}) = 0.5$. Consequently, the ratio of the non-stoichiometric *O* defect concentration and the total *Al* defect concentrations $(c(V_{Al@O_h})+c(V_{Al}))$ can be either $\frac{c(V_O)}{c(V_{Al@O_h})+c(V_{Al})} = \frac{1}{2+0} = \frac{1}{2} = 0.5$ or $\frac{c(V_O)}{c(V_{Al@O_h})+c(V_{Al})} = \frac{0}{2+1} = \frac{0}{3} = 0$ depending on the kind of the non-stoichiometric defect.

Solid-states nuclear magnetic resonance (NMR) measurements can predict atomic and electronic structures of materials using their responses to external magnetic fields [54]. NMR measurements have shown that the vacancies can be siuated in both sites, with almost 63% for the tetrahedral site and 37% for the octahedral site [55]. Gutiérrez and coworkers [34] using the pseudopotential method have analyzed 153 configurations for the possible positions of the two stoichiometric *Al* vacancies in the ideal γ-Al_2O_3 and proved that there are only 14 inequivalent configurations. They using their accurate DFT calculations have shown that the cation vacancies are located on the octahedral sites [34]. However, one should note that they have used a limited supercell in their calculations, and further investigations using larger supercells may provide more accurate results. It is also possible that at finite temperature the *Al* vacancies are located on tetrahedral sites. In our work, we have also introduced the non-stoichiometric *Al* and *O* defects in addition to the two stoichiometric *Al* defects in the ideal γ-Al_2O_3 crystal structure. This makes more complicated the determination of the positions of the defects in different sites. In this case, much more configurations in a bigger supercell should be considered to find the optimal structure with minimum total energy. However, investigation of different configurations with a large number of inequivalent atoms is extremely time-consuming and requires much more expensive calculations. Z. Li et al. using comprehensive *ab initio* calculations and studing the chemical potential dependence of defect formation energy of intrinsic point defects in $Y_4Al_2O_9$ (YAM) [56] and in yttrium aluminum garnet (YAG) [57] have shown that by changing the chemical potential environment it is possible to control the species of predominant intrinsic point defects. Thus, it is worth to mention that all these evidences show that further studies are demanded to check the dependence of the results on our assumptions used for the locations of the vacancies following the work reported in Ref. [34].

3. Computational details

All our calculations are carried out by the reliable WIEN2k code [58] to solve self-consistently the scalar-relativistic Kohn-Sham equations based on the density functional theory using the augmented plane waves plus local orbitals (APW + lo) method. For the exchange-correlation term, the generalized gradient approximation (GGA) is used. The bandgap calculations are improved by the TB-mBJ method. The bandgap is further improved by performing non-regular TB-mBJ calculations using the optimized c-factor (c_{opt}). In the non-regular, the *c*-factor of the (regular) TB-mBJ method is optimized to c_{opt}. The c_{opt} was found to be 1.8 for the ideal γ-Al_2O_3 [41]. We have recently observed the success of this method for fcc-C_{60} compound [59]. Our used computational parameters and details of regular and non-regular TB-mBJ calculations for the ideal structure are given in Fig. 1 (e) and were discussed in details in our previous work [41]. In this work, we use those parameters introduced in [41] and perform GGA and non-regular TB-mBJ with $c_{opt} = 1.8$ calculations for the defective spinel structures in the presence of the intrinsic point defects V_{Al4}, V_{Al6}, V_{O3}, and V_{O4}, see Fig. 2(a)–(d) as given and discussed in Sec. 2.2, respectively. After introducing each vacancy, the ions are allowed to relax until the forces are less than 1 mRy/Bohr. The calculations were performed by applying both GGA and mBJ-GGA methods, as implemented in the WIEN2k code [58].

4. Electronic structure

4.1. Band structures and subbands generated by intrinsic defects

The calculated band structure for the ideal defective spinel structure using the TB-mBJ method with $c_{opt} = 1.8$ is compared with those of the non-ideal structures in Fig. 3. The Fermi energies are calculated for the compounds under study and the results in *Ry* are presented in Table 1. The table shows that the calculated Fermi energies depend on the compounds and the applied approximations. However, only changes in energy are significant, hence, the

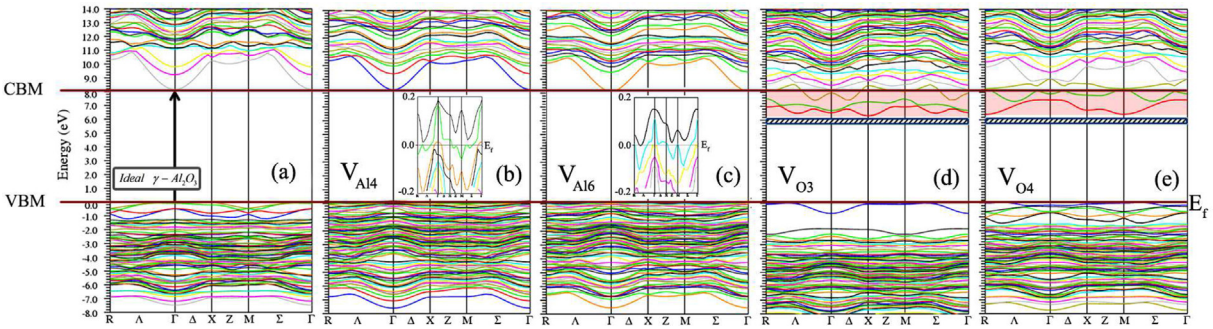

Fig. 3. "(color online)" Calculated band structures within the TB-mBJ for the (a) ideal structure, and the defective spinel structure in the presence of the intrinsic point defects (b) V_{Al4}, (c) V_{Al6}, (d) V_{O3}, and (e) V_{O4}. Inset figures represent the magnified bands in the vicinity of E_F for the cases of V_{Al4} and V_{Al6}. The colored ribbons show the calculated subbands originated from V_{O3} and V_{O4}. The hatched regions indicate the experimental trap centers, see Ref. [50]. V stands for vacancy and numbers are used to show the coordination numbers. Fermi level in *eV* is set to zero. (For interpretation of the references to color in this figure legend, the reader is referred to the Web version of this article.)

Table 1
Calculated Fermi energy in *Ry* for the ideal and defective cases.

Case	Approx.	$E_F(Ry)$
γ-Al_2O_3 (Ideal)	PBE-GGA	0.47
	TB-mBJ	0.65
γ-$Al_2O_3 + V_{O3}$	PBE-GGA	0.58
	TB-mBJ	0.74
γ-$Al_2O_3 + V_{O4}$	PBE-GGA	0.52
	TB-mBJ	0.64

point where one chooses the Fermi energy to be zero is arbitrary. The choice of the Fermi energy is arbitrary, but once one makes it, one must obviously maintain that choice consistently throughout the problem. When dealing with the band structures in the unit of *eV* by WIEN2k code, the code adjusts automatically E_F to zero for convenience. This is not the case in WIEN2k code, if one plots the band structures in the unit of *Ry*. In the latter case, the E_F is adjusted to the calculated Fermi level in *Ry*. It is obvious that the bandgap, the location of VBM, the location of CBM, the bands separations, and the overall shape of the bands are found to be exactly the same as each others by these two band offset methods and do not depend on the fact that E_F is set to zero *eV* or to the calculated nonzero E_F in *Ry*. Here, for convenience we have used the first band offset selection by plotting band structures in *eV* and adjusting E_F to zero. The result for the ideal structure, as plotted in Fig. 3 (a), shows a direct bandgap of 8.02 *eV* at Γ-point [41] which is in agreement with the experimentally reported bandgap [60] of 8.7 eV. It is worthwhile to mention here that the computational cost of the TB-mBJ calculations is of the same order as that of the standard LDA [61]. Besides, in some electronic structure calculations, the experimental total bandgap of the ideal γ-Al_2O_3 is assumed to be 7.2 *eV* [62], which is reported by French [63,64]. However, French has measured this bandgap in a polycrystalline γ-Al_2O_3 structure (γ-Al_2O_3 ceramic). It has been shown experimentally that, for an ideal and dense γ-Al_2O_3 structure, the total bandgap is ∼ 8.7 *eV* [65]. The bands of the ideal case, discussed in Ref. [41], is reproduced as a criterion to realize the effects of intrinsic point defects. In Fig. 3, the VBM and CBM of the ideal structure are indicated as two reference lines. By VBM and CBM we mean VBM and CBM of the ideal case in this paper. The band structures of the system in the presence of the V_{Al4}, V_{Al6}, V_{O3}, and V_{O4} intrinsic point defects are calculated within the TB-mBJ with $c_{opt} = 1.8$. The latter results are shown in Fig. 3(b) and (c), (d), and (e), respectively. The band structures in the presence of the *Al* vacancies, i.e., V_{Al4} (see Fig. 3 (b)) and V_{Al6} (see Fig. 3 (c)), show that extra bands, i.e., subbands, are produced by the defects V_{Al4} and V_{Al6}. For simplicity, the positions of the produced subbands in the presence of the vacancies are measured with respect to the VBM and CBM. The subbands are located around the Fermi level (E_F) below VBM in the valence region and above VBM in the bandgap region. The bands are magnified in the vicinity of E_F, as shown in the insets of Fig. 3(b) and (c) including the subbands. The insets show that the subbands are acceptor-like and distributed up to about 0.2 eV above the VBM or E_F in this case. The positions of the subbands with respect to the VBM are in excellent agreement with those of the G_0W_0 method [49]. It has been already observed that the vacancies are dominated more in the case of oxygen than aluminum in materials with high dielectric constants [44,66]. The band structure in the presence of V_{O3} is shown in Fig. 3 (d), while in the presence of V_{O4} is shown in Fig. 3 (e). The comparison of Fig. 3(b) and (c) with Fig. 3(d) and (e) shows that the effects of oxygen defects on the ideal band structure, as shown in Fig. 3 (a), are substantially different from those of the aluminum defects. The generated subbands by V_{O3} and V_{O4} are highlighted by two colored ribbons in Fig. 3(d) and (e), respectively. Experimental trap centers [50] are shown by hatched regions in Fig. 3(d) and (e), see also Ref. [49]. The colored ribbons, as our calculated subbands, lie in the bandgap region but this time close to the CBM. From Fig. 3(d) and (e), it is interesting to note that the calculated subbands are very close to the experimental hatched region. Therefore, our result shows that the subbands are distributed between ~0.4 and ~1.9 *eV* below the CBM. It has been experimentally observed that the defect bands are generated between ~1.9 and ~2.1 *eV* below the Al_2O_3 conduction band edge [50]. The *O* vacancies are experimentally predominant in γ-Al_2O_3 [44,49,66]. Thus, the natural defect subbands are mainly originated from the *O* vacancies compared to *Al* vacancies. This indicates that it is more reasonable to compare the induced subbands in the presence of *O* vacancies than that of *Al* vacancies with the experimental data. This verifies that our calculated positions of the subbands due to the V_{O3} and V_{O4} defects with respect to the CBM are in agreement with the experimental results, see Fig. 3(d) and (e) and Fig. 6 (a) of Ref. [50]. The V_{O3} and V_{O4} affect the ideal band structure. Our results show that the effect of V_{O3} is considerably different from that of V_{O4} at least in the valence region, see Fig. 3(d) and (e). The results show that some bands are removed from valence region close to E_F after introducing V_{O3} vacancy. The blank space of the removed bands can be clearly seen in Fig. 3 (d). This is not the case for V_{O4} vacancy, Fig. 3 (e). We shall subsequently in Sec. 4.2 discuss why V_{O3} and V_{O4} behave differently and have different effects on the valence bands of the ideal system.

4.2. Total DOS's and subbands generated by intrinsic defects

In order to elucidate the difference between V_{O3} and V_{O4}, as sketched at the end of Sec. 4, it is enough to shed light into the DOSs of the ideal and non-ideal systems. Fortunately, we recently calculated [41] total and partial DOSs for the ideal defective spinel structure within the TB-mBJ with $c_{opt} = 1.8$. Thereby, let us first briefly pick up from Ref. [41] only those results that are mandatory to complete the discussion of the different effects of V_{O3} and V_{O4} on the valence states right before the E_F. The total DOS and total p-DOSs for all of the non-equivalent *O* and *Al* atoms in the ideal

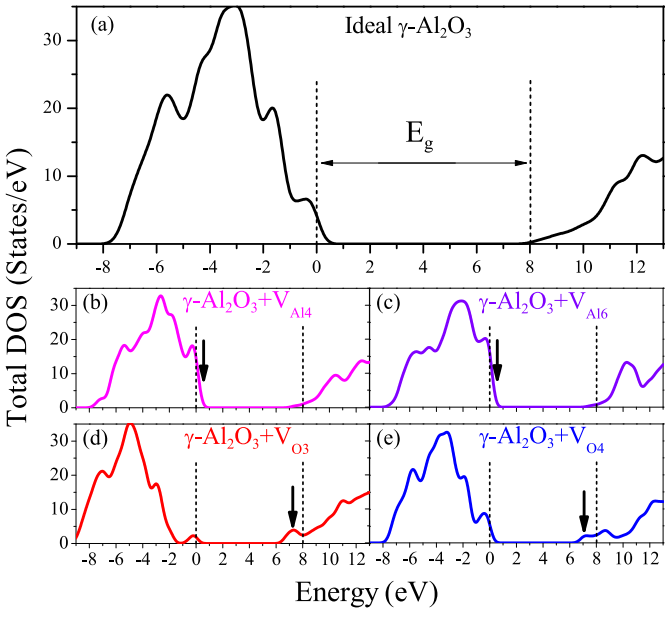

Fig. 4. "(color online)" Calculated total DOSs within the TB-mBJ for the (a) ideal structure, and the defective spinel structure in the presence of the intrinsic point defects (b) V_{Al4}, (c) V_{Al6}, (d) V_{O3}, and (e) V_{O4}. V stands for vacancy and numbers are used to show the coordination numbers. Fermi level in *eV* is set to zero.

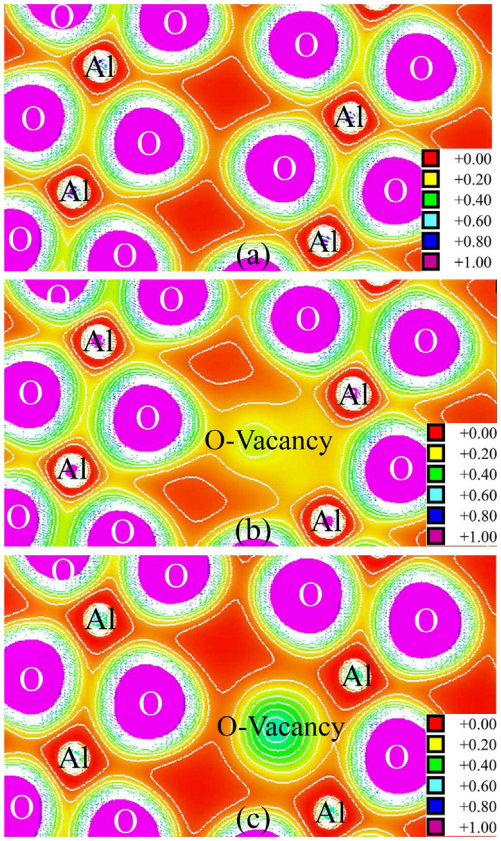

Fig. 5. "(color online)" Calculated electron charge density for the (a) ideal structure within the PBE-GGA, and for the defective spinel structure in the presence of the intrinsic point defects V_{O3} within the (b) PBE-GGA and (c) TB-mBJ.

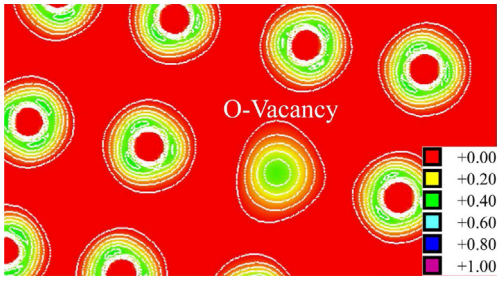

Fig. 6. "(color online)" Difference between the calculated electron charge densities (ECD's) by TB-mBJ and PBE-GGA, i.e., $ECD(TB-mBJ)-ECD(PBE-GGA)$, for the defective spinel structure in the presence of the intrinsic point defects V_{O3} by subtracting Fig. 5 (c) from Fig. 5 (b).

structure (not shown here) revealed that valence states right before the E_F were predominated by *O* p-states so that contributions of *Al* atoms in the total valence DOS close to the E_F were almost negligible (see Fig. 2 (a), (c), and (d) of Ref. [41]). It was also shown [41] that, among the non-equivalent *O* atoms, those of *O* atoms that were close to the vacancy of the ideal structure contributed more substantially in the valence states close to the E_F than those of *O* atoms that were far from the vacancy of the ideal structure, see Fig. 2(e) and (f) of Ref. [41]. The coordination number is 4 (3) for the first kind (second kind) of *O* atoms which are far from (close to) the vacancy of the ideal structure. Hence, the vacancy of the first kind (second kind) of *O* atoms is nothing more than what is denoted by V_{O4} (V_{O3}) in Sec. 2.2. As mentioned above, contributions of the second kind of *O* atoms to the valence states in the vicinity of E_F are much higher than the negligible contributions of the first kind of *O* atoms, see Fig. 2(e) and (f) of Ref. [41]. Thus, it is natural to observe blank space in the valence region close to E_F after removing the second kind of *O* atoms or forming the V_{O3}, see Fig. 3 (d). Inversely, one does not expect to see such a blank space (in the valence region close to the VBM) by forming the V_{O4}, V_{Al4}, and V_{Al6}, since their corresponding atoms do not strongly contribute right below the VBM region. The latter point is clearly verified by Fig. 3 (e), (b), and (c). Consequently in essence, we predict that the effects of V_{O3} and V_{O4} may not be similar on the valence states. Of course, we should note that the result obtained by V_{O3} can be considered similar to that of V_{O4}, if we only notice that the positions of the induced subbands by these two oxygen defects are close to each other; the generated subbands are placed right below the CBM. The total DOSs for the non-ideal structure in the presence of the *Al* and *O* defects are calculated within the TB-mBJ with $c_{opt}=1.8$. The results together with the total DOS for the ideal structure (for comparison) are shown in Fig. 4. The induced acceptor-like (donor-like) subbands by forming the V_{Al4} and V_{Al6} (V_{O3} and V_{O4}) are indicated by down-arrows in Fig. 4(b) and (c) (Fig. 4(d) and (e)), respectively. The positions of the latter acceptor-like (donor-like) subbands are consistent with Fig. 3(b) and (c) (Fig. 3(d) and (e)). The blank space in the valence region due to the formation of V_{O3} defects in the vicinity of E_F can be clearly seen in Fig. 4 (d). This is consistent with Fig. 3 (d). The generated subbands by V_{Al4} and V_{Al6} defects are close to each other and placed right above the VBM, see Fig. 4(b) and (c) or the insets shown in Fig. 3(b) and (c). Similarly, the generated subbands by V_{O3} and V_{O4} defects are placed right below the CBM, see Fig. 4(d) and (e) or the colored ribbons shown in Fig. 3(d) and (e). The total DOS of the system in the presence of the V_{O4} are more similar to the total DOS of the ideal system in valence region, see Fig. 4 (a) and (e). This is not the case for the conduction region. This shows that the V_{O4} affects the conduction states of the ideal system more strongly than the valence states. Inversely, total DOS of the system in the presence of the V_{Al4} are more similar to the total DOS of the ideal system in the conduction region, which is not the case in the valence region. This shows that the V_{Al4} affects the valence states of the ideal system more strongly than the conduction states of the ideal system. Neither in valence region nor in the conduction region, total V_{Al6} DOS is similar to the total DOS of the ideal system, see Fig. 4 (a) and (c). Similarly, total V_{O3} DOS is not similar to the total DOS of the ideal system in valence and conduction regions, see Fig. 4 (a) and (d).

4.3. Electron charge density within PBE-GGA and TB-mBJ

The electron charge density is calculated for the ideal γ-Al_2O_3 compound within the PBE-GGA. The PBE-GGA results are presented in Fig. 5 (a) for the ideal case. In order to introduce the oxygen vacancy in the system, i.e., V_{O3}, one of the oxygen atoms is removed from the ideal case. Then, we calculate the electron charge density for the defective spinel structure in the presence of the intrinsic point defect V_{O3} within the PBE-GGA. The PBE-GGA results are shown in Fig. 5 (b) for the γ-Al_2O_3 in the presence of the V_{O3}. The empty space of the removed oxygen atom can be clearly seen in Fig. 5 (b). However, the electron charge density is not completely vanished at the position of the oxygen vacancy, see Fig. 5 (b). The electron charge densities are quantitatively provided in $e/\text{Å}^3$ in the right hand side of the figures. It should be noted that the values are attributed to single colors, whereas in the figures there are mixed colors. For instance, around the V_{O3} vacancy, we have a mixed yellow and red colors. Thus, the electron charge densities around V_{O3} vacancy should be smaller than what is indicated for the yellow color, i.e., 0.2 $e/\text{Å}^3$. At this stage, we recalculate the electron charge density for the defective spinel structure in the presence of the

intrinsic point defect V_{O3} within the TB-mBJ with $c_{opt} = 1.8$, and the results are given Fig. 5 (c). It is clear from the plot that the electron charge density around V_{O3} vacancy is almost equal to the indicated value for the green color, i.e., $0.4\, e/\text{Å}^3$. This value, as predicted by the TB-mBJ, appears to be larger than that of the PBE-GGA, $0.2\, e/\text{Å}^3$. In order to ensure the correctness of the results, the TB-mBJ electron charge density, ECD(TB-mBJ), is subtracted from the PBE-GGA electron charge density, ECD(PBE-GGA). The difference between these two electron charge densities, i.e., ECD(TB-mBJ) - ECD(PBE-GGA), is obtained and plotted in Fig. 6. It is evident form the figure that the electron charge density in the position of the oxygen vacancy is made denser by the TB-mBJ than the PBE-GGA. It is interesting to note that the magnitude of ECD(TB-mBJ) - ECD(PBE-GGA) at the position of the oxygen vacancy has still considerable value of $\approx 0.4\, e/\text{Å}^3$, see green color at *O* vacancy in Fig. 6. The magnitude of ECD(TB-mBJ) - ECD(PBE-GGA) in the vicinity of the *O* vacancy decreases to around $\approx 0.2\, e/\text{Å}^3$ corresponding to the yellow color and gradually vanishes far from the *O* vacancy, see red color in Fig. 6. This shows that the predicted ECD by PBE-GGA at the position and in the vicinity of the oxygen vacancy is considerably smaller than the predicted ECD by TB-mBJ. The ECD(TB-mBJ) - ECD(PBE-GGA) becomes zero at the positions of the *O* and *Al* atoms and most of the other remaining regions except for the vicinity of the *O* and *Al* atoms, as can be clearly seen in Fig. 6. The calculated higher and denser electron charge density around the oxygen vacancy by the TB-mBJ confirms that the TB-mBJ is a superior theoretical technique than PBE-GGA for the calculation of the positions of the subbands. Therefore, the TB-mBJ can predict the donor subbands more accurately than PBE-GGA. But, we should recall that this satisfactory result of the TB-mBJ is indebted to the optimized *c*-factor, i.e., $c_{opt} = 1.8$.

5. Conclusions

The effects of the intrinsic *Al* and *O* point defects on the band structures of γ-Al_2O_3 compound are investigated by the density functional theory utilizing the PBE-GGA and TB-mBJ. Our results show that the oxygen defects have considerable effects on the band structure of the ideal γ-Al_2O_3 and should be taken into account. The band structures of the system in the presence of the defects reveal additional acceptor- and donor-like sublevels. The positions of the sublevels which are produced by the defects are found to be in agreement with the experimental observations. Both PBE-GGA and TB-mBJ predict correctly that oxygen vacancies introduce donor-like subbands below the CBM. It is found that the non-regular TB-mBJ method predicts the positions of the subbands more accurately than the PBE-GGA. The non-regular TB-mBJ predicts that the effects of V_{O3} and V_{O4} on the valence states are not similar to each other. The positions of the subbands which are predicted accurately by the TB-mBJ are crucial, as they may be used in prediction of the physical properties such as optical transitions.

Acknowledgment

This work is supported by the University of Isfahan, Isfahan, Iran.

References

[1] M.S. Lavine, A revealing view of oxides, Science 360 (6384) (2018) 45–46, https://doi.org/10.1126/science.360.6384.45-e. http://science.sciencemag.org/content/360/6384/45.5.

[2] S. Demchyshyn, J. M. Roemer, H. Groiß, H. Heilbrunner, C. Ulbricht, D. Apaydin, A. Böhm, U. Rütt, F. Bertram, G. Hesser, M. C. Scharber, N. S. Sariciftci, B. Nickel, S. Bauer, E. D. Głowacki, M. Kaltenbrunner, Confining metal-halide perovskites in nanoporous thin films, Science Advances 3 (8). URL http://advances.sciencemag.org/content/3/8/e1700738.

[3] C.K. Narula, L.F. Allard, Z. Wu, Ab initio density functional calculations and infra-red study of co interaction with pd atoms on θ-al 2 o 3 (010) surface, Sci. Rep. 7 (1) (2017) 6231.

[4] R. Mondragón, J.E. Juliá, L. Cabedo, N. Navarrete, On the relationship between the specific heat enhancement of salt-based nanofluids and the ionic exchange capacity of nanoparticles, Sci. Rep. 8 (1) (2018) 7532.

[5] A.A. Gonçalves, M.J. Costa, L. Zhang, F. Ciesielczyk, M. Jaroniec, One-pot synthesis of meal2o4 (me= ni, co, or cu) supported on γ–$Al_2O_3$with ultralarge mesopores: enhancing interfacial defects in -γal2o3 to facilitate the formation of spinel structures at lower temperatures, Chem. Mater. 30 (2) (2018) 436–446.

[6] D. Christensen, Y. Frenkel, P. Schütz, F. Trier, S. Wissberg, R. Claessen, B. Kalisky, A. Smith, Y. Chen, N. Pryds, Electron mobility in γ- al 2 o 3/srtio 3, Physical Review Applied 9 (5) (2018), 054004.

[7] C. Freysoldt, B. Grabowski, T. Hickel, J. Neugebauer, G. Kresse, A. Janotti, C.G. Van de Walle, First-principles calculations for point defects in solids, Rev. Mod. Phys. 86 (2014) 253–305, https://doi.org/10.1103/RevModPhys.86.253. http://link.aps.org/doi/10.1103/RevModPhys.86.253.

[8] A. Nourmohammadi, S.J. Asadabadi, M.H. Yousefi, M. Ghasemzadeh, Photoluminescence emission of nanoporous anodic aluminum oxide films prepared in phosphoric acid, Nanoscale Research Letters 7 (1) (2012) 689.

[9] C.-H. Zhang, B. Chen, Y. Jin, D.-B. Sun, A dft study on the failure mechanism of γ–Al_2O_3film by various point defects in solution, Chem. Phys. 504 (2018) 48–56.

[10] L. Chen, Y. Zhang, X. Wang, B. Jalan, S. Chen, Y. Hou, The roles of point defects in thermal transport in perovskite barium stannate, J. Phys. Chem. C. 122 (21) (2018) 11482–11490.

11 C.E. Dreyer, A. Alkauskas, J.L. Lyons, A. Janotti, C.G. Van de Walle, First-principles calculations of point defects for quantum technologies, Annu. Rev. Mater. Res. Annu. Rev. Mater. Res. 48 (2018), 2.1.

[12] R. Stern, T. Wang, J. Carrete, N. Mingo, G.K. Madsen, Influence of point defects on the thermal conductivity in fesi, Phys. Rev. B 97 (19) (2018) 195201.

[13] W.-D. Zabka, D. Leuenberger, G. Mette, J. Osterwalder, From two- to three-dimensional alumina: interface templated films and formation of γ–Al_2o_3(111) nuclei, Phys. Rev. B 96 (2017) 155420, https://doi.org/10.1103/PhysRevB.96.155420. https://link.aps.org/doi/10.1103/PhysRevB.96.155420.

[14] J. Wilt, Y. Gong, M. Gong, F. Su, H. Xu, R. Sakidja, A. Elliot, R. Lu, S. Zhao, S. Han, J.Z. Wu, Atomically thin Al_2O_3films for tunnel junctions, Phys. Rev. Applied 7 (2017), 064022, https://doi.org/10.1103/PhysRevApplied.7.064022. https://link.aps.org/doi/10.1103/PhysRevApplied.7.064022.

[15] M. Koberidze, M.J. Puska, R.M. Nieminen, Structural details of Al/Al_2O_3-junctions and their role in the formation of electron tunnel barriers, Phys. Rev. B 97 (2018) 195406, https://doi.org/10.1103/PhysRevB.97.195406. https://link.aps.org/doi/10.1103/PhysRevB.97.195406.

[16] Y.K. Wakabayashi, Y. Nonaka, Y. Takeda, S. Sakamoto, K. Ikeda, Z. Chi, G. Shibata, A. Tanaka, Y. Saitoh, H. Yamagami, M. Tanaka, A. Fujimori, R. Nakane, Electronic structure and magnetic properties of magnetically dead layers in epitaxial $CoFe_2O_4$/Al_2O_3/Si(111)films studied by x-ray magnetic circular dichroism, Phys. Rev. B 96 (2017) 104410, https://doi.org/10.1103/PhysRevB.96.104410. https://link.aps.org/doi/10.1103/PhysRevB.96.104410.

17 P. Samanta, J. Leszczynski, High-temperature thermoelectric transport behavior of al/γ–Al_2O_3 interface: impact of electron and phonon scattering at nanoscale metal-ceramic contacts, Phys. Chem. Chem. Phys. 20 (2018) 14513–14524.

[18] M.R. Zemła, P. Śpiewak, T. Wejrzanowski, K.J. Kurzydłowski, Hydrophobic properties of γ–Al_2O_3doped with rare-earth metals: ab initio modeling studies, Phys. Status Solidi A 215 (2018) 1700895.

[19] S. Na-Phattalung, S. Limpijumnong, T. Jiraroj, J. Yu, et al., Magnetic states and intervalence charge transfer of ti and fe defects in α-Al_2O_3: the origin of the blue in sapphire, Acta Mater. 143 (2018) 248–256.

[20] L. Fu, H. Yang, Tailoring the electronic structure of mesoporous spinel -al2o3 at atomic level: Cu-doped case, J. Phys. Chem. C 118 (26) (2014) 14299–14315, https://doi.org/10.1021/jp502204h. http://pubs.acs.org/doi/abs/10.1021/jp502204h.

[21] H. Papi, S. Jalali-Asadabadi, A. Nourmohammadi, I. Ahmad, J. Nematollahi, M. Yazdanmehr, Optical properties of ideal γ–$Al_2O_3$and with oxygen point defects: an ab initio study, RSC Adv. 5 (68) (2015) 55088–55099.

[22] S.G. Higgins, M.M. Stevens, Extracting the contents of living cells, Science 356 (6336) (2017) 379–380, https://doi.org/10.1126/science.aan0228. http://science.sciencemag.org/content/356/6336/379.

[23] R.A. Rahardi, R. Maharsi, F. Iskandar, H. Devianto, Y.W. Budhi, Catalytic oxidation of benzene using nano-cuo/γ-al2o3 and commercial catalysts, in: IOP Conference Series: Earth and Environmental Science, vol. 105, IOP Publishing, 2018, 012039.

[24] S. Tabesh, F. Davar, M.R. Loghman-Estarki, Preparation of γ-al2o3 nanoparticles using modified sol-gel method and its use for the adsorption of lead and cadmium ions, J. Alloy. Comp. 730 (2018) 441–449.

[25] R. Li, H. Chen, Z. Gan, M. Jiang, A. Zhong, H. Bao, Bimetallic ag–ru/γ-Al_2O_3 nanoparticles for selective hydrogenation of cinnamaldehyde to hydrocinnamaldehyde, Micro & Nano Lett. 13 (2) (2018) 243–247.

[26] M.-C. Lu, C.-H. Huang, Specific heat capacity of molten salt-based alumina nanofluid, Nanoscale Research Letters 8 (1) (2013) 292, https://doi.org/10.1186/1556-276X-8-292. https://doi.org/10.1186/1556-276X-8-292.

[27] N. Nikolaou, P. Dimitrakis, P. Normand, D. Skarlatos, K. Giannakopoulos, K. Mergia, V. Ioannou-Sougleridis, K. Kukli, J. Niinist, K. Mizohata, M. Ritala, M. Leskel, Inert ambient annealing effect on manos capacitor memory characteristics, Nanotechnology 26 (13) (2015) 134004. http://stacks.iop.org/

0957-4484/26/i=13/a=134004.
[28] Y. Zhou, S.-T. Han, P. Sonar, V. Roy, Nonvolatile multilevel data storage memory device from controlled ambipolar charge trapping mechanism, Sci. Rep. 3 (2013) 2319.
[29] C. Zhao, C.Z. Zhao, S. Taylor, P.R. Chalker, Review on non-volatile memory with high-k dielectrics: flash for generation beyond 32 nm, Materials 7 (7) (2014) 5117–5145, https://doi.org/10.3390/ma7075117. http://www.mdpi.com/1996-1944/7/7/5117.
[30] A. Padovani, A. Arreghini, L. Vandelli, L. Larcher, G. Van den Bosch, P. Pavan, J. Van Houdt, A comprehensive understanding of the erase of tanos memories through charge separation experiments and simulations, Electron Devices, IEEE Transactions on 58 (9) (2011) 3147–3155, https://doi.org/10.1109/TED.2011.2159722.
[31] M. Zahid, A. Arreghini, R. Degraeve, B. Govoreanu, A. Suhane, J. Van Houdt, Electron trap profiling near/gate interface in tanos stack using gate-side trap spectroscopy by charge injection and sensing, Electron Device Letters, IEEE 31 (10) (2010) 1158–1160, https://doi.org/10.1109/LED.2010.2057239.
[32] C.-H. Lee, S.-H. Hur, Y.-C. Shin, J.-H. Choi, D.-G. Park, K. Kim, Charge-trapping device structure of sio2sinhigh-k dielectric al2o3 for high-density flash memory, Appl. Phys. Lett. 86 (15) (2005) 152908. https://doi.org/10.1063/1.1897431. http://scitation.aip.org/content/aip/journal/apl/86/15/10.1063/1.1897431.
[33] Y.J. Seo, K.C. Kim, H.D. Kim, M.S. Joo, H.M. An, T.G. Kim, Correlation between charge trap distribution and memory characteristics in metal/oxide/nitride/oxide/silicon devices with two different blocking oxides, al2o3 and sio2, Appl. Phys. Lett. 93 (6) (2008), 063508, https://doi.org/10.1063/1.2970990. https://doi.org/10.1063/1.2970990.
[34] G. Gutiérrez, A. Taga, B. Johansson, Theoretical structure determination of $\gamma-al_2o_3$, Phys. Rev. B 65 (2001), 012101, https://doi.org/10.1103/PhysRevB.65.012101. http://link.aps.org/doi/10.1103/PhysRevB.65.012101.
[35] H.P. Pinto, R.M. Nieminen, S.D. Elliott, Ab initio, Phys. Rev. B 70 (2004) 125402, https://doi.org/10.1103/PhysRevB.70.125402. http://link.aps.org/doi/10.1103/PhysRevB.70.125402.
[36] E. Menéndez-Proupin, G. Gutiérrez, Electronic properties of bulk γ-al_2o_3, Phys. Rev. B 72 (2005), 035116, https://doi.org/10.1103/PhysRevB.72.035116. http://link.aps.org/doi/10.1103/PhysRevB.72.035116.
[37] C.-K. Lee, E. Cho, H.-S. Lee, K.S. Seol, S. Han, Comparative study of electronic structures and dielectric properties of alumina polymorphs by first-principles methods, Phys. Rev. B 76 (2007) 245110, https://doi.org/10.1103/PhysRevB.76.245110. http://link.aps.org/doi/10.1103/PhysRevB.76.245110.
[38] W.Y. Ching, L. Ouyang, P. Rulis, H. Yao, Ab initio, Phys. Rev. B 78 (2008), 014106, https://doi.org/10.1103/PhysRevB.78.014106. http://link.aps.org/doi/10.1103/PhysRevB.78.014106.
[39] V.V. Afanas'ev, M. Houssa, A. Stesmans, C. Merckling, T. Schram, J.A. Kittl, Influence of $\gamma-Al_2O_3$crystallization on band offsets at interfaces with si and tinx, Appl. Phys. Lett. 99 (7) (2011), 072103. https://doi.org/10.1063/1.3623439. http://scitation.aip.org/content/aip/journal/apl/99/7/10.1063/1.3623439.
[40] R. Ahuja, J.M. Osorio-Guillen, J.S. de Almeida, B. Holm, W.Y. Ching, B. Johansson, Electronic and optical properties of ? - al 2 o 3 from ab initio theory, J. Phys. Condens. Matter 16 (16) (2004) 2891. http://stacks.iop.org/0953-8984/16/i=16/a=013.
[41] M. Yazdanmehr, S.J. Asadabadi, A. Nourmohammadi, M. Ghasemzadeh, M. Rezvanian, Electronic structure and bandgap of $\gamma-Al_2O_3$compound using mbj exchange potential, Nanoscale Research Letters 7 (1) (2012) 488.
[42] J. Gu, J. Wang, J. Leszczynski, Structure and energetics of (111) surface of $\gamma-Al_2O_3$: insights from dft including periodic boundary approach, ACS Omega 3 (2) (2018) 1881–1888.
[43] A.S. Jbara, Z. Othaman, H. Aliabad, M. Saeed, Investigation of electronic and optical properties of $\gamma-$and α-alumina by first principle calculations, Adv. Sci. Lett. 24 (5) (2018) 3579–3581.
[44] D. Liu, J. Robertson, Oxygen vacancy levels and interfaces of $\gamma-Al_2O_3$, Microelectron. Eng. 86 (79) (2009) 1668–1671. https://doi.org/10.1016/j.mee.2009.03.011. http://www.sciencedirect.com/science/article/pii/S0167931709001762.
[45] A.I. Kostyukov, A.V. Zhuzhgov, V.V. Kaichev, A.A. Rastorguev, V.N. Snytnikov, V.N. Snytnikov, Photoluminescence of oxygen vacancies in nanostructured $\gamma-Al_2O_3$, Opt. Mater. 75 (2018) 757–763. https://doi.org/10.1016/j.optmat.2017.11.040. http://www.sciencedirect.com/science/article/pii/S0925346717307395.
[46] V. Pustovarov, T. Perevalov, V. Gritsenko, T. Smirnova, A. Yelisseyev, Oxygen vacancy in $\gamma-Al_2O_3$: photoluminescence study and first-principle simulation, Thin Solid Films 519 (19) (2011) 6319–6322. https://doi.org/10.1016/j.tsf.2011.04.014. http://www.sciencedirect.com/science/article/pii/S0040609011008261.
[47] G. Molas, M. Bocquet, E. Vianello, L. Perniola, H. Grampeix, J. Colonna, L. Masarotto, F. Martin, P. Brianceau, M. Gly, C. Bongiorno, S. Lombardo, G. Pananakakis, G. Ghibaudo, B.D. Salvo, Reliability of charge trapping memories with high-k control dielectrics (invited paper), Microelectron. Eng. 86 (79) (2009) 1796–1803. https://doi.org/10.1016/j.mee.2009.03.083. http://www.sciencedirect.com/science/article/pii/S0167931709002482.
[48] C. Cheng, S. Adegbite, J. Oladejo, Microstructural properties and grinding of $\gamma-\gamma-Al_2O_3$and coal for environmental applications, Part. Sci. Technol. (2018) 1–7.
[49] K. Sankaran, G. Pourtois, R. Degraeve, M.B. Zahid, G.-M. Rignanese, J. Van Houdt, First-principles modeling of intrinsic and extrinsic defects in ?-$\gamma-Al_2O_3$, Appl. Phys. Lett. 97 (21) (2010) 212906. https://doi.org/10.1063/1.3507385. http://scitation.aip.org/content/aip/journal/apl/97/21/10.1063/1.3507385.
[50] R. Degraeve, M. Cho, B. Govoreanu, B. Kaczer, M.B. Zahid, J. Van Houdt, M. Jurczak, G. Groeseneken, Trap spectroscopy by charge injection and sensing (tscis): a quantitative electrical technique for studying defects in dielectric stacks, in: Electron Devices Meeting, 2008. IEDM 2008, IEEE International, 2008, pp. 1–4, https://doi.org/10.1109/IEDM.2008.4796812.
[51] F. Tran, P. Blaha, Accurate band gaps of semiconductors and insulators with a semilocal exchange-correlation potential, Phys. Rev. Lett. 102 (2009) 226401.
[52] M. Sun, A.E. Nelson, J. Adjaye, Examination of spinel and nonspinel structural models for $\gamma-Al_2O_3\gamma-Al_2O_3$by dft and rietveld refinement simulations, J. Phys. Chem. B 110 (5) (2006) 2310–2317, https://doi.org/10.1021/jp056465z, pMID: 16471818, http://pubs.acs.org/doi/abs/10.1021/jp056465z.
[53] G.H. Vineyard, G.J. Dienes, The theory of defect concentration in crystals, Phys. Rev. 93 (1954) 265–268, https://doi.org/10.1103/PhysRev.93.265. https://link.aps.org/doi/10.1103/PhysRev.93.265.
[54] J. Nematollahi, S. Jalali-Asadabadi, Microscopic sources of solid-state nmr shielding in titanate of alkaline earth perovskite metals, J. Phys. Chem. C 122 (36) (2018) 20589–20601. https://doi.org/10.1021/acs.jpcc.8b05356.
[55] M.-H. Lee, C.-F. Cheng, V. Heine, J. Klinowski, Distribution of tetrahedral and octahedral a1 sites in gamma alumina, Chem. Phys. Lett. 265 (6) (1997) 673–676. https://doi.org/10.1016/S0009-2614(96)01492-3. http://www.sciencedirect.com/science/article/pii/S0009261496014923.
[56] Z. Li, B. Liu, J. Wang, L. Sun, J. Wang, Y. Zhou, Z. Hu, First-principles study of point defects in stoichiometric and non-stoichiometric y4al2o9, J. Mater. Sci. Technol. 29 (12) (2013) 1161–1165. https://doi.org/10.1016/j.jmst.2013.10.004. http://www.sciencedirect.com/science/article/pii/S1005030213002314.
[57] Z. Li, B. Liu, J. Wang, L. Sun, J. Wang, Y. Zhou, Mechanism of intrinsic point defects and oxygen diffusion in yttrium aluminum garnet: first-principles investigation, J. Am. Ceram. Soc. 95 (11) (2012) 3628–3633, https://doi.org/10.1111/j.1551-2916.2012.05440.x. https://ceramics.onlinelibrary.wiley.com/doi/pdf/10.1111/j.1551-2916.2012.05440.x. https://ceramics.onlinelibrary.wiley.com/doi/abs/10.1111/j.1551-2916.2012.05440.x.
[58] P. Blaha, K. Schwarz, G.K.H. Madsen, D. Kvasnicka, J. Luitz, WIEN2k: an Augmented Plane Waves Plus Local Orbitals Program for Calculating Crystal Properties, Vienna University of Technology, Austria, 2001.
[59] S. Jalali-Asadabadi, E. Ghasemikhah, T. Ouahrani, B. Nourozi, M. Bayat-Bayatani, S. Javanbakht, H.A.R. Aliabad, I. Ahmad, J. Nematollahi, M. Yazdani-Kachoei, Electronic structure of crystalline buckyballs: fcc-c60, J. Electron. Mater. 45 (1) (2016) 339–348, https://doi.org/10.1007/s11664-015-4080-2. https://doi.org/10.1007/s11664-015-4080-2.
[60] B. Ealet, M. Elyakhloufi, E. Gillet, M. Ricci, Electronic and crystallographic structure of ?-alumina thin films, Thin Solid Films 250 (12) (1994) 92–100. https://doi.org/10.1016/0040-6090(94)90171-6. http://www.sciencedirect.com/science/article/pii/0040609094901716.
[61] D. Koller, F. Tran, P. Blaha, Improving the modified becke-johnson exchange potential, Phys. Rev. B 85 (2012) 155109, https://doi.org/10.1103/PhysRevB.85.155109. http://link.aps.org/doi/10.1103/PhysRevB.85.155109.
[62] G. Pourtois, K. Sankaran, I. Radu, R. Degraeve, M.B. Zahid, S. Van Elshocht, C. Adelmann, S. De Gendt, M.M. Heyns, D.J. Wouters, J.A. Kittl, M. Jurczak, G.-M. Rignanese, J. Van Houdt, (invited) first-principles investigation of high-k dielectrics for nonvolatile memories, ECS Transactions 33 (3) (2010) 393–407, https://doi.org/10.1149/1.3481628. http://ecst.ecsdl.org/content/33/3/393.abstract.
[63] R.H. French, Electronic band structure of $\gamma-Al_2O_3$, with comparison to alon and ain, J. Am. Ceram. Soc. 73 (3) (1990) 477–489, https://doi.org/10.1111/j.1151-2916.1990.tb06541.x. https://doi.org/10.1111/j.1151-2916.1990.tb06541.x.
[64] R.H. French, H. Müllejans, D.J. Jones, Optical properties of aluminum oxide: determined from vacuum ultraviolet and electron energy-loss spectroscopies, J. Am. Ceram. Soc. 81 (10) (1998) 2549–2557, https://doi.org/10.1111/j.1151-2916.1998.tb02660.x. https://doi.org/10.1111/j.1151-2916.1998.tb02660.x.
[65] V.V. Afanas'ev, A. Stesmans, B.J. Mrstik, C. Zhao, Impact of annealing-induced compaction on electronic properties of atomic-layer-deposited $\gamma-Al_2O_3$, Appl. Phys. Lett. 81 (9) (2002) 1678–1680. https://doi.org/10.1063/1.1501163. http://scitation.aip.org/content/aip/journal/apl/81/9/10.1063/1.1501163.
[66] J. Robertson, High dielectric constant gate oxides for metal oxide si transistors, Rep. Prog. Phys. 69 (2) (2006) 327. http://stacks.iop.org/0034-4885/69/i=2/a=R02.